LAWRENCE
LIVERMORE
NATIONAL
LABORATORY

UCRL-JRNL-225790

Impedancemetric NOx Sensing Using Yttria-Stabilized Zirconia (YSZ) Electrolyte and YSZ/Cr2O3 Composite Electrodes

L P Martin, L. Y. Woo, R. S. Glass

November 2, 2006

Journal of the Electrochemical Society

Disclaimer

Impedancemetric NO_x sensing using YSZ electrolyte and YSZ/Cr_2O_3 composite electrodes

L. Peter Martin[a,c], Leta Y. Woo[b,*], and Robert S. Glass[b,*]

[a] Mechanical Engineering Directorate and [b]Energy and Environment Directorate

Lawrence Livermore National Laboratory, P.O. Box 808, Livermore, CA 94551

ABSTRACT

An impedancemetric method for NO_x sensing using an yttria-stabilized zirconia (YSZ) based electrochemical cell is described. The sensor cell consists of a planar YSZ electrolyte and two identical YSZ/Cr_2O_3 composite electrodes exposed to the test gas. The sensor response to a sinusoidal ac signal applied between the two electrodes is measured via two parameters calculated from the complex impedance, the modulus |Z| and phase angle Θ. While either of these parameters can be correlated to the NO_x concentration in the test gas, Θ was found to provide a more robust metric than |Z|. At frequencies below approximately 100 Hz, Θ is sensitive to both the NO_x and O_2 concentrations. At higher frequencies, Θ is predominantly affected by the O_2 concentration. A dual frequency measurement is demonstrated to compensate for changes in the O_2 background between 2 and 18.9%. Excellent sensor performance is obtained for NO_x concentrations in the range of 8-50 ppm in background. An equivalent circuit model was used to extract fitting parameters from the impedance spectra for a preliminary analysis of NO_x sensing mechanisms.

[c]Corresponding author: Phone: 925-423-9831, Fax: 925-423-7040, email: martin89@llnl.gov

[*]Electrochemical Society Active Member

Keywords: NO_x, stabilized zirconia, electrochemical sensor, impedancemetric

Introduction

Increasingly stringent emissions regulations will require the development of advanced gas sensors for a variety of applications. For example, compact, inexpensive sensors are needed for detection of regulated pollutants, including hydrocarbons (HC), CO, and NO_x, in automotive exhaust. Because many emerging applications, particularly monitoring of automotive exhaust, involve operation in harsh environments, which can include high temperature and corrosive or chemically reactive conditions, ceramic oxide-based electrochemical sensors have received considerable interest. Sensors using yttria-stabilized zirconia (YSZ) as an oxygen ion conducting electrolyte have been widely reported for both amperometric and potentiometric modes of operation.[1,2] The most successful of these sensors is probably the well-known Exhaust Gas Oxygen (EGO) sensor.

YSZ-based amperometric sensors have been reported for detection of low concentrations of various gasses including hydrocarbon (HC), NO_x, CO, and humidity.[3-11] Amperometric sensors can be configured as NO-selective or total-NO_x sensors, and significant recent efforts have gone into the investigation of various metal-oxide electrodes to optimize the sensing response.[3,8,9,12] Because the O_2 pumping current is measured as the sensing signal, these sensors are generally quite sensitive to the O_2 concentration. This effect can be compensated by separate measurement of the O_2 concentration, or by using a multi-chamber device with a separate pumping cell to maintain a constant O_2 concentration at the sensing electrode.[13-16] Also, there is some indication that the O_2 sensitivity can be mediated by proper selection of the electrode materials and configuration.[17,18] A commercially available amperometric sensor has been reported to detect total NO_x at concentrations above ~100 ppm in automobile exhaust, but has poor sensitivity at lower concentrations.[15,16]

Potentiometric sensors operate by measurement of the open-circuit potential (OCP) between two dissimilar electrodes (alternatively, two similar electrodes with one of them situated in a fixed reference gas). With proper electrode selection, typically Pt reference and metal-oxide sensing electrodes, the reaction kinetics at the two electrodes can be made sufficiently different as to result in a measurable potential difference which can be correlated to the gas composition. This type of sensor is often referred to as a 'mixed potential' sensor because the oxygen potentials at the two electrodes are established by reactions with NO and NO_2 (or other oxygenated gas species), as well as with O_2.[9,19] Alternatively, there has been some discussion of differential electrode equilibria which are not strictly described by the 'mixed potential' model due to considerations related to the electronic (semiconducting) properties of the metal-oxide electrode.[20,21]

Potentiometric sensors can exhibit high sensitivity to low concentrations of various species including NO_x, CO, HC, and H_2.[22-27] Sensors using electrodes based on spinel or perovskite oxides have been reported for NO_x sensing, and the capability to detect <100 ppm NO_x at temperatures as high as 700°C is well established.[28-30] However, the response to NO_2 is generally opposite (in sign) to, and larger than, the NO response, which presents certain complications for sensor operation in 'real-world' applications. In addition, the open-circuit measurement provides little control over the effect of interfering gasses, and anecdotal evidence seems to indicate that acceptable response times can be difficult to achieve at temperatures that are low enough to give sufficient sensitivity.

Recently, an ac impedance-based technique has been reported for sensing NO_x, CO, HC, and humidity using a YSZ electrolyte and various electrode materials.[31-35] In the impedancemetric technique, changes in the complex impedance of the sensor are measured as the

sensing signal. A total-NO_x sensor has been reported which uses a tubular YSZ electrolyte, $ZnCr_2O_4$ sensing electrode, and a Pt/air reference electrode.[32] The modulus of the impedance, |Z|, is measured at 1 Hz as the sensing signal at 600-700^oC. This operating frequency was selected as a compromise between increased response (at lower frequency), and decreased noise and sampling time (at higher frequency). In a follow-on work, a planar YSZ configuration was demonstrated for a CO sensor using an Au-Ga_2O_3 sensing electrode.[34] Once again, the sensing signal was provided by measurement of |Z| at 1 Hz.

The present work presents an impedancemetric NO_x sensor consisting of a planar YSZ electrolyte and YSZ/Cr_2O_3 composite electrodes attached with Au leads. The electrodes were nominally identical, and are both exposed to the test gas (i.e., no air reference). Impedance spectra are presented and the NO_x sensing mechanism is evaluated within the context of an equivalent circuit model. NO_x sensing is performed by monitoring the impedance (|Z|) and phase-angle (Θ). For the current sensor configuration, the Θ response provides higher sensitivity and better stability. It is shown that the sensitivity to the O_2 concentration at 10 Hz can be compensated using data from a second measurement frequency (1000 Hz) where the response to NO_x is limited but the response to O_2 is robust.

Experimental

Sensor fabrication - The sensor was fabricated by coating composite electrodes onto a YSZ electrolyte. The electrolyte was prepared from YSZ (Tosoh 8-YS) by pressing in a uniaxial die and sintering at 1450^oC for 2 hours. Electrodes were applied by spray coating 10% Cr_2O_3 (by weight) / 90% YSZ onto the YSZ substrate. The electrode geometry consisted of two side-by-side rectangular electrodes on the same side of the electrolyte separated by approximately 0.5

mm. The area of each electrode was 28 mm^2. After deposition, the electrodes were fired at 1000°C for one hour. Fig. 1 shows SEM micrographs of a fracture surface from an electrode. The images show a fine, interconnected network of YSZ particles, approximately 100 nm in diameter, surrounding isolated (non-percolated) particles of Cr_2O_3, that are approximately 500 nm in size. The electrode thickness was approximately 7.5 μm.

Sensor testing - Sensor testing was performed in a quartz tube heated in a tube furnace to 600°C. In the test configuration, both electrodes were exposed to the gas flow, i.e. there is no external reference electrode, and the gas composition was controlled by mixing air, N_2, and 1000 ppm NO or NO_2 in N_2 using a standard gas handling system equipped with thermal mass flow controllers. Gas flow rate was maintained at 500ml/min for all compositions. A dense Au foil was overlaid on top of the sensor electrodes to provide electrical contact (i.e., as a current collector). To insure uniform and effective contact, the foil was held in place by an Al_2O_3 flat placed on top of the foils and spring-loaded to apply a constant pressure. Electrochemical measurements were performed using a Solartron 1260 impedance analyzer and the ZPlot software. Impedance spectra were acquired using an excitation voltage of 50 mV_{rms} by stepping the frequency from 100 kHz to 0.1 Hz, with a frequency resolution of 20 steps/decade. The spectra were analyzed using the Boukamp EQUIVCRT.COM software.

Results and Discussion

Impedance spectroscopy - Fig. 2 shows a Nyquist plot of the impedance spectrum for the sensor at 600°C in 10.5% O_2. Also shown are the spectra for 100 ppm concentrations of NO and NO_2 at the same O_2 concentration. Points corresponding to 0.1, 1.0, 10, 100, and 1000 Hz

are marked on each spectrum. Two arcs were observed within the frequency range explored; a small arc at high frequencies above approximately 100 kHz (too small to be visible in the Figure), and a large arc visible in the Figure below 1 kHz. The high frequency arc is attributed to the bulk YSZ electrolyte (i.e., conductivity and dielectric constant) and is insensitive to variations in the O_2 and NO_x concentrations. The low frequency arc, the diameter of which is significantly reduced with the introduction of either NO or NO_2, is attributed to electrode and interface processes. The non-ideal shape (i.e., deviation from semi-circular arcs) of the low frequency arc could indicate heterogeneities in bulk and interfacial properties and/or a convolution of various processes such as diffusion, charge transfer, and adsorption/desorption.

Miura, et al.,[31,32] and Wu, et al.,[34] have seen qualitatively similar impedance behavior using $ZnCr_2O_4$ sensing electrodes to detect NO_x and Au-Ga_2O_3 sensing electrodes to detect CO, respectively. The response using a $ZnCr_2O_4$ electrode was attributed to possible changes in the electrode-interface resistance due to reactions occurring at the interface. It should be noted that in their study, the counter electrode was Pt and was exposed to atmospheric air, while only the sensing electrode was exposed to the test atmosphere with different concentrations of NO_x. For the CO sensor, the Au- Ga_2O_3 sensing electrode and Pt reference electrode were both exposed to the same test atmosphere, and the impedance behavior was attributed to changes in charge transfer kinetics at the electrolyte/electrode interface.

A preliminary equivalent-circuit analysis of the Nyquist data from Fig. 2 was performed in order to provide insight into the operating mechanism(s) of the present sensor. The equivalent circuit model shown in Fig. 2 (inset) was fit to each of the spectra using Boukamp's EQUIVCRT.COM program. The model consists of a series resistance, R_S, which accounts bulk contributions from the YSZ, a fractal Gerischer (FG) element, and a subcircuit consisting of a

resistor, R_{LF}, and a constant phase element (CPE) in parallel. The CPE accounts for heterogeneities introduced by the non-ideal behavior of real systems and has the following impedance relationship[36]

$$Z(w) = \frac{1}{Y_o(jw)^n} \quad (1)$$

where for n = 1 the impedance reduces to a capacitor with a value of Y_o. The fractal Gerischer has the following impedance relationship[37,38]

$$Z(w) = \frac{1}{Y_o(k + jw)^m} \quad (2)$$

When m = 0.5 the expression reduces to a Gerischer impedance, which implies an electrochemical reaction preceded and followed by a chemical reaction with an effective transfer rate equal to k. Similar to the n-parameter for the constant phase element, values of m < 0.5 in the FG account for heterogeneities in the non-ideal behavior of real systems.[37,38] The best fit of the equivalent circuit to the three spectra are shown as the solid lines in Fig. 2.

Table I shows the best-fit parameters for each of the spectra in Fig. 2. The Table shows the changes associated with the NO_x response to be dominated by the R_{LF}-CPE subcircuit. With the addition of 100 ppm of either NO or NO_2, R_{LF} decreases by ~25% and $Y_{o,LF}$ decreases by ~8.5%, with no significant change in the n-parameter. While the fractal Gerischer parameters also change, it is important to note that at the frequencies of interest the overall contribution from the FG is significantly smaller than the contribution from R_{LF} and the CPE. As an example, at low frequencies the effective resistance associated with the fractal Gerischer can be approximated as

$$R_{FG} = \frac{1}{Y_o k^m} \quad (3)$$

Using the values for $Y_{o,LF}$, k, and m from Table I, this relation predicts the associated resistance change for the fractal Gerischer to be ~850 Ω with the addition of either 100 ppm of NO or NO_2. In contrast, the change in R_{LF} is approximately ~12 kΩ with the same NO_x addition. Because the largest changes occur in the R_{LF}-CPE subcircuit, the NO_X-sensing response is attributed to the physical processes occurring at the electrode surface and electrode-electrolyte interface.[36]

As will be discussed below, the current sensor can resolve single-digit ppm levels of NO_x in O_2 concentrations as high as 18.9%. In the presence of O_2 and NO_x, the following electrochemical reactions are known to occur at the triple-phase boundary

$$NO + O^{2-} \Leftrightarrow NO_2 + 2e^- \quad (4)$$

$$1/2O_2 + 2e^- \Leftrightarrow O^{2-} \quad (5)$$

Both reactions occur simultaneously, with relative rates that are dependant upon surface morphology and chemistry, as well as triple phase boundary characteristics. The observed sensor response can be described, within the context of these simultaneous O_2 and NO_x reactions, by proposing that (4) and (5) occur via parallel reaction pathways. R_{LF} can therefore be stated as

$$R_{LF} = \left[\frac{1}{R_{O_2}} + \frac{1}{R_{NO_x}} \right]^{-1} \quad (6)$$

where R_{O2} and R_{NOx} are the respective resistances associated with the O_2 and NO_x reaction paths. The form of Eq. (6) places requires the relative magnitudes of R_{O2} and R_{NOx} to be within approximately two orders of magnitude of one another for the larger resistance term to have a significant effect upon R_{LF}. To attempt to resolve the relative contributions of these two terms we investigated to slight modifications of the sensor configuration.

In the first configuration, the YSZ-Au interface was modified by inserting a layer of porous Au between the dense Au and the porous YSZ. This was accomplished by ‘painting’ a

layer of unfritted Au-ink onto the surface of the dense Au and firing at 900°C for 1 hour. The net effect was to increase the relative amount of Au surface area near the triple phase boundary. The resultant cell impedance decreased dramatically and became completely insensitive to the presence of NO_x in the high O_2 backgrounds evaluated here (2-18.9%). The O_2 response was qualitatively the same as with the dense Au plate but with a decreased overall impedance. Within the context of the parallel path model, these observations indicate that the increased Au surface area preferentially enhances the O_2 reaction, thus changing the relative magnitude of R_{O2} and R_{NOx} so that they are no longer sufficiently close to allow the changes in R_{NOx} to be resolved in R_{LF}. The results also indicate that R_{NOx} is the higher resistance of the two terms. In the second modified configuration, the Au collector was replaced with a dense Pt plate. The observed effect was qualitatively the same as with the introduction of the porous Au: lower overall impedance and negligible NO_x response (at 2-18.9% O_2). Because Pt is a more efficient O_2 catalyst than Au, and because it is known that O_2 and NO compete for adsorption sites on the Pt surface[39], the implication is again that the Pt collector preferentially enhances the O_2 reaction. Within the context of the parallel reaction path model, this creates a condition where the O_2 reaction is sufficiently lower in resistance than the NO_x reaction to enable it to overwhelm the NO_x response.

These tests of the modified sensor configurations indicate that by adding more surface area (Au) or a better O_2 catalyst (Pt) the NO_x response is suppressed in the presence of significant concentrations of O_2. This is interpreted within the parallel reaction path model as resulting from the preferential enhancement of the O_2 reaction over the NO_x reaction, and the resultant decrease in R_{O2} relative to R_{NOx} in Eq. (6). Ref. 40 discusses a more detailed analysis of a similar sensor/cell, identical in structure and fabrication to that used in the present work

except that the electrodes are 100% YSZ rather than 90% YSZ / 10%Cr_2O_3.[40] The investigation of the sensing mechanism performed in ref. 40 includes equivalent circuit analysis of impedance spectra acquired at a variety of O_2 and NO_x concentrations. Such an analysis is beyond the scope of this manuscript, however efforts are ongoing to further elucidate the sensing mechanisms.

From a sensor application standpoint, the implication of these observations is that an effective sensor configuration utilizes a combination of structure and materials which leads comparable resistance for the O_2 and NO_x reactions. The resultant effect of NO_x on R_{LF} can be correlated to the NO_x concentration. However, that would require acquiring a significant portion of the Nyquist plot and numerically extracting the desired measurement. Since this is not a viable methodology for a compact sensor system, it is of interest to explore a more experimentally accessible measurement parameter, for example the modulus |Z|, or the phase Θ. These are related to the complex impedance Z

$$Z = Z' + jZ'' \tag{7}$$

by

$$\begin{aligned} |Z| &= \sqrt{Z'^2 + Z''^2} \\ \Theta &= \arctan\left(\frac{Z''}{Z'}\right) \end{aligned} \tag{8}$$

or, conversely

$$\begin{aligned} Z' &= |Z|\cos(\Theta) \\ Z'' &= |Z|\sin(\Theta) \end{aligned} \tag{9}$$

Fig. 3a shows the Bode plots of |Z| and Θ for the same impedance spectra shown in Fig. 2. It is interesting to note that the response in Θ associated with the presence of NO_x persist to significantly higher frequency than does the response in |Z|. Mathematically, this is a result of the fact that |Z| is calculated from the sum of the squares of Z' and Z", while Θ is calculated from

the ratio. The facts that the NO_x response is only a small fraction of the overall magnitude of Z' or Z", and that over most of the frequency range of interest Z' >> Z" (refer to Fig. 2), also contribute to the effect. The shift in Θ also decays to zero as the frequency approaches zero (dc). The net result is that the effect of NO_x on Θ reaches a maximum at approximately 2 Hz before decaying slowly with increasing frequency. In contrast, the |Z|-response is largest at dc, and decreases rapidly with increasing frequency.

The responses of |Z| and Θ to NO are illustrated more clearly in Fig. 3b, where ΔΘ and Δ|Z| are plotted versus frequency to show the effect of 100 ppm NO relative to the 10.5% O_2 baseline. Fig. 3b shows that the phase shift due to the NO addition reaches a maximum at 2 Hz, and decays with increasing frequency to reach 90 and 71% of the maximum value at 5 and 10 Hz, respectively. In contrast, the maximum measured shift in |Z| is at the lowest frequency sampled (0.1 Hz). From Fig. 2, it is expected that |Z| will continue to increase as the frequency approaches zero, at which point it will reach the dc resistance. |Z| decays with increasing frequency at all frequencies above zero, and this decay can be seen to be notably faster than for the Θ response. For example, at 5 and 10 Hz the shift in |Z| has decayed to 43 and 21%, respectively, of the value at 2 Hz (these values are given for comparison with the Θ data), and to 17 and 7.5%, respectively, of the maximum measured shift at 0.1 Hz.

In the prior work cited above, impedancemetric-type sensors were operated at 1 Hz frequency as a compromise between sensitivity and sampling rate.[32,33] In addition, those studies used |Z| as the sensing measurement. However, Fig.3b implies the capability for operation at higher frequency, and with potentially higher sampling rates, using Θ than |Z| as the sensing signal. In addition, inspection of Eq. (8) will show that the effective contributions of Z' and Z" (and therefore the measured in- and out-of phase current) to |Z| must always be additive.

Therefore, any transient noise, or thermal or age-related drift, in either term must always manifest in |Z|. In contrast, because Θ is related to the ratio of Z' and Z", and thus to the ratio of the in- and out-of phase current, the possibility exists for some amount of 'canceling' provided the two terms vary similarly. This is in fact what is observed, as will be discussed below where it will be shown that the Θ response has a better signal-to-noise ratio and is more stable than the |Z| response. For that reason, Θ was selected as the sensing parameter for the sensor. It should be noted that the overall sensing methodology is not contingent upon using Θ as the sensing parameter. However, our observations, as delineated in the discussion above, are that the measurement parameter should be related to the ratio of the real and imaginary terms to provide the best possibility for high stability and signal-to-noise.

The viability of using Θ for measurement of the NO_x concentration at frequencies significantly higher than 1 Hz has important implications for 'real-world' sensor applications. Increased operating frequency typically presents the opportunity for improved signal processing (i.e., noise correction), faster sensor response time, and reduced sampling time (time between measurements). Also, as can be seen from Figs. 2 and 3a, at frequencies above ~100 Hz the NO_x response is negligible. This presents an additional opportunity to implement a multiple-frequency mode of operation to allow for compensation from interfering effects such as fluctuating O_2 concentration and variations in temperature. The data presented in the next section will demonstrate how sensor operation at two distinct frequencies can be utilized to correct for wide variations in the O_2 concentration while maintaining high sensitivity to NO_x. A sensing frequency of 10 Hz was selected as a compromise between increased sensitivity (at lower frequency) and reduced sampling time/improved signal-to-noise (at higher frequency). This represents potentially an order of magnitude faster sampling rate than previous reports,

while maintaining the capability to resolve sub-10 ppm levels of NO_x.

Impedancemetric NO_x sensing - Fig. 4a shows Θ and |Z| measured during continuous operation at 10 Hz using a 50 mV excitation voltage. The data show the sensor response as the O_2 concentration is cycled through the sequence 10.5, 2.0, 7.0, 10.5, and 18.9%. These O_2 concentrations are indicated in the Figure, and the sensor response to the changing concentrations is clearly apparent. At each concentration, NO_x exposures are performed by introducing 50, 25, 15, and 8 ppm NO followed by the same levels of NO_2. The responses to these NO_x additions are the stair-step signals superimposed on the O_2 response curve. Several aspects of these data are immediately apparent. The response to NO and NO_2 are comparable in magnitude, with the NO response being slightly larger. This is consistent with the impedance spectra shown in Fig. 2 and 3a. The Θ response to the NO_x exposures is significantly more pronounced than the |Z| response at all O_2 concentrations, with 8 ppm of NO_x clearly resolvable. This is illustrated more clearly in Fig. 4b, which shows an expanded view of the NO_x response in 10.5% O_2 from Fig. 4a. Relative to |Z|, the Θ response is faster and more stable over the course of the measurements. The sharp transient at the beginning of the NO_2 exposure is an experimental artifact related to residual NO in the shared gas line. As stated above, the improved stability of Θ relative to |Z| is attributed to its dependence upon the ratio of Z" to Z'.

Fig. 5 is identical to Fig. 4a, except that the measurement frequency has been increased to 1000 Hz. At this increased frequency the sensor shows no response to NO_x in either Θ or |Z|. The implication of the effect is that the O_2 and NO_x have different dominant reaction pathways, and that these pathways have different frequency dependence. While this is consistent with the parallel reaction path model proposed above, it is not currently possible to provide a detailed

mechanistic explanation as to why the NO_x reaction pathway should abate more rapidly with increasing frequency than the O_2 pathway. It is noteworthy, however, that the response to changes in the O_2 concentration shows qualitatively the same behavior to that observed during 10 Hz operation, albeit with a reduced amplitude. In fact, this similarity is sufficient to allow compensation of the baseline (i.e., zero NO_x) measured at 10 Hz for the effects of changes in the O_2 concentration. Fig. 6 shows Θ(10 Hz) measured at the end of each of the O_2 concentration steps (2, 7, 10.5, and 18.9%) from Fig. 4a plotted versus Θ(1000 Hz) measured at those same points in Fig. 5. A least squared regression fit shows a high linearity over most of the concentration range (7.0 - 18.9%). The deviation of the datum for 2.0% O_2 is a result of the slow O_2 response of the sensor, as a result of which Θ fails to equilibrate in the time of the measurement and thus contains some residual (transient) offset related to the measurement made at the preceding O_2 concentration. Efforts are currently underway to further evaluate methodologies for improving the speed of the O_2 response.

As mentioned above, the linear correlation between the Θ measured at 10 and 1000 Hz as a function of the O_2 concentration can be directly implemented to compensate the Θ(10 Hz) for the effects of changing O_2 concentration, thus allowing extraction of the NO_x concentration. This is done by using the linear least squares regression analysis of the data in Fig. 5,

$$\Theta(10Hz) = 3.18 \cdot \Theta(1000Hz) + 61.68 \qquad (8)$$

to calculate an O_2-dependent, but *NO_x-independent*, baseline at 10 Hz from the O_2-dependent but NO_x independent Θ(1000 Hz). In other words, the Θ measured at 1000 Hz, Θ(1000 Hz), is input into Eq. (8) to predict Θ(10 Hz), in the absence of NO_x. Since the measured Θ(10 Hz) is sensitive to both NO_x and O_2, the difference between the measured Θ(10 Hz) and that calculated from Eq. (8) yields the NO_x response. The result of this analysis is shown in Fig. 7, where the

data from Fig. 4a have been numerically (point-by-point) corrected for the O_2 response using Eq. (8) and the data from Fig. 5. The analysis yields excellent compensation for the O_2 concentration at 7.0, 10.5, and 18.9% O_2, with clear resolution of 8 ppm levels of both NO and NO_2 at all three O_2 concentrations. At the lowest O_2 concentration, 2.0%, the results are not as accurate, however this can be attributed to the slow O_2 response for this sensor, as previously discussed, and should be resolved by modifying the materials or structure to facilitate a faster O_2 response. It should be noted that the measurements at the two frequencies were not made simultaneously, but rather concurrently. As a result, some interpolation and time shifting had to be performed in order to align the data temporally for the analysis. This leads to transient effects were the signal changes rapidly, for example where the O_2 concentration is stepped in Fig. 7. In a real application, it is envisioned that measurement process would be implemented by simultaneous excitation of the sensor using a mixed signal containing components at both frequencies (10 and 1000 Hz), thus allowing real-time correction and reducing transient artifacts associated with the data time-shifting.

The NO response time was evaluated for the data in Figure 7. The results are tabulated in Table II, which shows the 90% response time, τ_{90}, when the NO concentration is stepped from 0 to 50 ppm, 50 to 25 ppm, and 8 to 0 ppm at each O_2 concentration. The τ_{90}, defined as the time required to reach 90% of the steady state value after the gas composition is changed, is <6 seconds under all conditions tested. This response time of a few seconds is considered reasonable for an initial effort in this type of sensor, and can likely be improved by modification of the sensor geometry. The response times from Table II are comparable to those seen in the uncompensated Θ measurements (Fig 4b), and the NO response in both cases (compensated and uncompensated) is on the order of 1000x faster than the response to changes in O_2 concentration

shown in Fig. 4b. Mechanistically, this is of interest because it implies that the NO and O_2 reactions occur by different pathways (with different rate limiting mechanisms) and thus supports the parallel path model proposed above.

The data from Fig. 7 are compiled in Figs. 8a and b, where the compensated sensor response is plotted as a function of the concentrations of NO and NO_2 for different baseline O_2 concentrations. An approximately linear relationship is found at all O_2 concentrations in the range of 2-18.9%. The measured sensitivities are 0.040 and 0.034 degrees/ ppm, for NO and NO_2, respectively, indicating a detection limit of <10 ppm NO_x. As expected, the response in 2% O_2 varies from that for the other concentrations due to the slow O_2 response. Initial cross-sensitivity testing indicates that the addition of ~2% (by volume) H_2O vapor shifts the baseline and reduces the NO sensitivity slightly. However, it is not currently clear what will be the effect of higher levels more comparable with those found in the automotive environment (5-15%). While these results clearly indicate that it is possible to detect low levels of NO_x in the laboratory, significant improvement will probably be necessary before the methodology can be deployed in a real application where more significant background noise will be apparent. In addition, ongoing efforts will evaluate the effects of interfering gasses including H_2O, hydrocarbons, urea and ammonia.

Effects of excitation voltage and aging - Fig. 9 shows the Nyquist plot for the sensor in 10.5% O_2, and with the addition of 100 ppm NO and NO_2, when the (ac) excitation amplitude is increased to 140 mV. In comparison to the data obtained at the lower excitation amplitude (50 mV, Fig. 2a), the data in Fig. 9 show that the increased amplitude results in a slight suppression of the arc diameters. The difference between the spectra at the two excitation frequencies is

attributed to nonlinear behavior of the cell at excitation voltages in excess of ~100 mV. This upper limit for linearity was determined by: i) evaluating current-voltage sweeps performed at various scan rates, and ii) scanning the excitation voltage from 10 mV to ~250 mV at a constant frequency (10 Hz). Evaluation of the sensing response was performed using the 140 mV excitation in order to determine the effect of exceeding the linear regime.

The Bode plot corresponding to Fig. 9 is shown in Fig. 10. The behavior is qualitatively similar to that in Fig. 3a, but shows a reduced NO_x response and a faster decay with increasing frequency. To evaluate the effect of the increased excitation voltage on NO_x sensing, impedancemetric measurements were made at 10 and 1000 Hz. The resultant data were comparable to Figs. 4a and 5. Analysis of the data was performed in the same way as for the lower excitation voltage (presented above) by determining an equation comparable to Eq. (8) based upon the measured O_2-dependent baselines at the two frequencies. The results are shown in Fig. 11, where the compensated Θ(10 Hz) is plotted versus time. Once again, the O_2 concentration is stepped through the sequence 2.0, 10.5, 7.0, and 18.9%, while at each concentration NO_x is introduced at levels of 50, 25, 15, and 8 ppm NO, followed by the same concentration sequence for NO_2.

The data shown in Fig. 11 are comparable to those in Fig. 7 in that the measurements made in 2% O_2 are offset due to the slow O_2 response of the sensor. It can be seen in Fig. 11 that the increased excitation voltage results in a reduced response relative to the 50 mV excitation (e.g., ~1.4^o versus 2.0^o for 50 ppm NO). It is also apparent that the background noise level is significantly reduced at the higher excitation voltage. The net result is a higher signal-to-noise ratio despite the reduction in absolute response. To illustrate this point, for each excitation amplitude the response to 50 ppm NO was compared with the rms background noise. This latter

value was determined by calculating the rms value for a suitable section of flat baseline (0 ppm NO_x) consisting of ~500 points. This ratio of signal to background increases from 95 to 125 as the excitation voltage increases from 50 to 140 mV. This is a significant improvement in the signal to noise ratio; however, with respect to a real application (i.e., on-board automotive) these laboratory data may not represent an achievable noise level, and therefore the tradeoff of response amplitude for baseline noise may or may not be attractive.

The data shown in Fig. 11 represent a 12-hour window of an extended period of continuous operation lasting 140 hours (e.g., hours 79 - 91). This extended testing was performed at the higher excitation voltage in order to expedite any electrochemical aging processes. During this extended operation, the NO_x exposure cycle shown in Fig.11 was repeated several times. The Θ(1000 Hz) measurements used for background compensation were acquired after the end of the 140hours, which is 50 hours after the end of the NO_x exposure in Fig. 11, and used to compensate all the NO_x exposure cycles. The result was a series of data plots comparable to Fig. 11, from which the NO response at 15, 25, and 50 ppm were determined at each O_2 concentration (except 2.0%). Fig. 12 shows the result of that analysis, where the baseline (0 ppm NO_x) and NO responses are plotted as a function of time for 7.0, 10.5 and 18.9% O_2. The data show a slight drift in the baseline and a similar drift in the NO response, both of which appear to stabilize after ~100hrs of operation. The source of this very small drift (approximately the equivalent of the response to 15 ppm NO over the course of the entire 140 hours) is not currently understood. Possible causes include aging of the sensor, drifting of the mass flow controllers used to control the gas composition, or slight changes in the furnace temperature.

It is interesting to note that there is some variation in the data with respect to the response

versus O_2 concentration. For example, note that at early times the largest response at all NO concentrations is in 18.9% O_2 (grey symbols), while the smallest is in 7% (filled symbols). At times times, this trend is reversed. At intermediate times, similar response is obtained at all O_2 concentrations. (Note that those data were used to generate the compensation.) This effect is completely consistent with a slight drift (over the 140hr experiment) of the Θ(10 Hz) baseline which is not necessarily matched by the Θ(1000 Hz) compensation data since the latter were only obtained only at the conclusion of the experiment. It is quite possible that if the 1000 Hz compensation data were simultaneously measured in real time along with the 10 Hz data, that the observed drift would occur at both frequencies and that the compensation would be even more effective.

Conclusions

A new impedancemetric method for NO_x sensing is described. The sensor consists of a planar YSZ electrolyte and two identical YSZ/Cr_2O_3 composite electrodes. Using ac impedance measurements, the NO_x concentration can be correlated with the measured |Z| or Θ. However, Θ appears to be more stable, and shows a higher sensitivity to NO_x (easily resolving 8 ppm NO_x). The response to NO_2 and NO are similar in magnitude, with the NO response being slightly larger. Under the conditions employed in this study, Θ measured at 10 Hz is sensitive to both NO_x and O_2 concentrations, while at 1000 Hz it is only sensitive to O_2. An algebraic relationship relating the measured Θ at the two frequencies relative to the changing O_2 concentration allows extraction of the NO_x concentration. Excellent sensor performance is obtained for NO_x concentrations in the range of 8-50 ppm. The response curve (ΔΘ versus NO_x concentration) is linear over entire the range for background O_2 concentrations ranging from 2-

18.9%. The response in 2% O_2 is offset from measurements at other O_2 concentration levels due to a slow sensor response to changing O_2. However, this is unlikely to be a problem for operation of the sensor in real applications where the anticipated O_2 levels are expected to be in the range of 6-15% (i.e., for diesel exhaust monitoring). The potential viability of the sensing method has significant implications for "real world" applications, including the opportunity for improved noise correction, faster sensor response time, and reduced sampling time.

While a detailed study of the NO_x sensing mechanism was beyond the scope of this work, a preliminary equivalent circuit analysis of the Nyquist data was performed. The largest changes in the impedance spectra with addition of NO_x to the test gas appear to be associated with changes in a low frequency resistive component and a constant phase element. Based on this, the response is attributed to the physical processes occurring at the electrode surface and electrode-electrolyte interface. More detailed characterization of the sensing mechanism for this type of sensor is currently under investigation. In addition, more exhaustive prototype testing is currently underway, including evaluation of the effects of interfering gasses (H_2O, hycrocarbon, ammonia) and testing in an automotive dynamometer exhaust.

Acknowledgments

This work was performed under the auspices of the U. S. Department of Energy by the University of California, Lawrence Livermore National Laboratory under Contract No. W-7405-Eng-48.

References

1. F. Menil, V. Coillard, and C. Lucat, *Sensors Actuators B*, **67**, 1 (2000).

2. W. Göpel, G. Reinhardt and M. Rösch, *Solid State Ionics*, **136-137**, 519 (2000).

3. S. Somov, G. Reinhardt, U. Guth and W. Göpel, *Sensors and Actuators B*, **35-36**, 409 (1996).

4. P. Schmidt-Zhang and U. Guth, *Sensors and Actuators B*, **99**, 258 (2004).

5. T. Ishihara, M. Fukuyama, A. Dutta, K. Kabemura, H. Nishiguchi and Y. Takita, *J. Electrochem. Soc.*, **150**, H241 (2003).

6. T. Hibino, Y. Kuwahara and S. Wang, *J. Electrochem. Soc.*, **146**, 382 (1999).

7. N. Miura, G. Lu, M. Ono and N. Yamazoe, *Solid State Ionics*, **117**, 283 (1999).

8. D.L. West, F.C. Montgomery and T.R. Armstrong, *Sensors and Actuators B*, **111-112**, 84 (2005).

9. V. Coillard, H. Debéda, C. Lucat and F. Ménil, *Sensors and Actuators B*, **78**, 113 (2001).

10. Y. Tan and T.C. Tan, *Sensors and Actuators B*, **28** 113 (1995).

11. H. Yagi and K. Ichikawa, *Sensors and Actuators B*, **13-14**, 92 (1993).

12. D.L. West, F.C. Montgomery and T.R. Armstrong, *J. Electrochem. Soc.*, **153**, H23 (2006).

13. S.I. Somov, G. Reinhardt, U. Guth and W. Göpel, *Solid State Ionics*, **136-137**, 543 (2000).

14. U. Nigge, H.-D. Wiemhöfer, E.W.J. Römer, H.J.M. Bouwmeester and T.R. Schulte, *Solid State Ionics*, **146**, 163 (2002).

15. N. Kato, H. Karachi, and Y. Hamada, SAE Tech. Paper Series No. 980170 (1998).

16. N. Kato, K. Nakagaki, and N. Ina, SAE Tech. Paper Series No. 960334 (1996).

17. David L. West, Fred C. Montgomery, and Timothy R. Armstrong, *J. Electrochem. Soc.*, **152**, H74 (2005).

18. K.-Y. Ho, M. Miyayama, and H. Yanagida, *J. Ceram. Soc. Jpn.*, **104**, 995 (1996).

19. F.H. Garzon, R. Mukundan and E. Brosha, *Solid State Ionics*, **136-137**, 633 (2000).

20. E. Di Bartolomeo, M.L. Grilli and E. Traversa, *J. Electrochem. Soc.*, **151**, H133 (2004).

21. E.D. Wachsman and P. Jayaweera, in *Solid State Ionic Devices II-Ceramic Sensors*, E.D. Wachsman, et al., eds. (The Electrochemical Society Proceedings Series, Pennington, NJ, 2001), p. 298.

22. L.P. Martin, Q. Pham and R. Glass, *Sensors and Actuators B*, **96**, 53 (2003).

23. L. P. Martin and R. S. Glass, *J. Electrochem. Soc.*, **152**, H43 (2005).

24. E.L. Brosha, R. Mukundan, D.R. Brown, F.H. Garzon, J. H. Visser, J.H. Zanini, Z. Zhou and E.M. Logethetis, *Sensors and Actuators B*, **69**, 171 (2000).

25. G. Lu, N. Miura, and N. Yamazoe, *Sensors and Actuators B*, **35**, 130 (1996).

26. R. Mukundan, E. Brosha, F.H. Garzon, *J. Electrochem. Soc.*, **150**, H279 (2003).

27. E.L. Brosha, R. Mukundan, D.R. Brown and F.H. Garzon, *Sensors and Actuators B*, **87**, 47 (2002).

28. E. Di Bartolomeo, N. Kaabbuathong, A. D'Epifanio, M.L. Grilli, E. Traversa, H. Aono,Y. Sadaoka, *J. of the European Ceram. Soc.*, **24**, 1187 (2004).

29. S. Zhuiykov, T. Nakano, A. Kunimoto, N. Yamazoe and N. Miura, *Electrochem. Comm.*, **3**, 97 (2001).

30. N. Miura, S. Zhuiykov, T. Ono, M. Hasei and N. Yamazoe, *Sensors and Actuators B*, **83**, 222 (2002).

31. M. Nakatou and N. Miura, *J. Ceram. Soc. Japan*, **112**, S532 (2004).

32. N. Miura, M. Nakatou and S. Zhuiykov, *Sensors and Actuators B*, **93**, 221 (2003).

33. M. Nakatou and N. Miura, *Solid State Ionics*, **176**, 2511 (2005).

34. N. Wu, Z. Chen, J. Xu, M. Chyu and S.X. Mao, *Sensors and Actuators B*, **110**, 49 (2005).

35. M. Nakatou and N. Miura, *Electrochem. Comm.*, **6**, 995 (2004).

36. J.R.Macdonald, *Impedance Spectroscopy: Emphasizing Solid Materials and Systems* (John Wiley and Sons, Inc., New York, 1987).

37. M. González-Cuenca, W. Zipprich, B.A. Boukamp, G. Pudmich and F. Tietz, *Fuel Cells*, **1**, 256 (2001).

38. B.A. Boukamp and H.J.M. Bouwmester, *Solid State Ionics*, **157**, 29 (2003).

39. T.M. Gür and R.A. Huggins, *J. Electrochem. Soc.*, **126**, 1067 (1979).

40. L.Y. Woo, L.P. Martin and R.S. Glass, submitted to *J. Electrochem. Soc.* (August, 2006).

Figure captions

Fig. 1: SEM micrographs of a fracture surface from a YSZ/Cr_2O_3 composite electrode.

Fig. 2: Nyquist plot showing the impedance spectrum for the sensor at 600^oC in 10.5% O_2 (triangles), and in 10.5% O_2 mixed with 100 ppm NO (circles) and 100 ppm NO_2 (squares). Solid lines show the best fit of the equivalent circuit (inset) to the spectra. The frequencies indicated are accurate for both the raw data and the total circuit.

Fig. 3a: Bode plot of the impedance spectrum for the sensor at 600^oC in 10.5% O_2 (solid lines), and in 10.5% O_2 mixed with 100 ppm NO (dotted lines) and 100 ppm NO_2 (dashed lines).

Fig. 3b: Difference between the Θ measured in 10.5% O_2, and in 10.5% O_2 mixed with 100 ppm NO, from Fig. 3a. Also shown, the difference between the |Z| measured in 10.5% O_2, and in 10.5% O_2 mixed with 100 ppm NO.

Fig. 4a: |Z| and Θ measured at 10 Hz and 600^oC with an excitation voltage of 50 mV rms. The O_2 concentration varies from 2 -18.9%, and NO_x exposures of 50, 25, 15, and 8 ppm of NO (1^{st}) and NO_2 (2^{nd}) are performed at each concentration.

Fig. 4b: Expanded view of the 1^{st} 100 minutes from Fig.3a. Shows |Z| and Θ measured at 10 Hz in 10.5% O_2. NO (1^{st}) and NO_2 (2^{nd}) concentrations are indicated in the Figure (50, 25, 15, and 8 ppm).

Fig. 5: |Z| and Θ measured at 1000 Hz and 600^oC with an excitation voltage of 50 mV rms. The O_2 concentration varies from 2 -18.9%, and NO_x exposures of 50, 25, 15, and 8 ppm of NO (1^{st}) and NO_2 (2^{nd}) are performed at each concentration. The gas concentration profile (versus time) is exactly the same as in Fig. 4a.

Fig. 6: Phase angle measured at 10 Hz, Θ(10 Hz), versus 1000 Hz, Θ(1000 Hz), for O_2 concentrations from 2 to 18.9%. The O_2 concentrations are indicated in the Figure. All

measurements were made at 600°C and 50 mV excitation voltage.

Fig. 7: Sensor response, Θ(10 Hz), from Fig. 4a compensated for the O_2 background using Θ(1000 Hz), versus from Fig. 5 and the linear correlation from Fig. 6.

Fig. 8: Compensated sensor response from Fig. 7, Θ(10 Hz, compensated), compiled to illustrate (a) NO and (b) NO_2 response at O2 concentrations of 2% (filled diamonds), 7% (open squares), 10.5% (filled triangles), and 18.9% (open diamonds).

Fig. 9: Nyquist plot showing the impedance spectrum for the sensor at 600°C in 10.5% O_2 (triangles), and in 10.5% O_2 mixed with 100 ppm NO (circles) and 100 ppm NO_2 (squares). The excitation voltage is 140 mV rms.

Fig. 10: Bode plot of the impedance spectrum for the sensor at 600°C in 10.5% O_2 (solid lines), and in 10.5% O_2 mixed with 100 ppm NO (dotted lines) and 100 ppm NO_2 (dashed lines). The excitation voltage is 140 mV rms.

Fig. 11: Phase response at 10 Hz compensated for the O_2 background using Θ(1000 Hz) with an excitation voltage of 140 mV.

Fig. 12: O_2-compensated phase response during 140 hours of continuous operation with an excitation voltage of 140 mV. Response to 0, 15, 25, and 50 ppm NO (diamond, square, triangle, and circle, respectively) are shown for 7, 10.5 and 18.9% O_2 (filled, open, and grey symbols, respectively).

Table I: Values for equivalent circuit model (Fig. 2b) at 50 mV. See text for details about the parameters.

		10.5% O_2	**10.5% O_2 + 100ppm NO**	**10.5% O_2 + 100ppm NO_2**
	R_s	504	489	489
Fractal Gerischer:	**$Y_{o,FG}$**	5.33E-05	5.92E-05	5.80E-05
	k	65	103	99
	m	0.31	0.30	0.30
Constant Phase Element:	**$Y_{o,LF}$**	3.17E-06	2.89E-06	2.92E-06
	n	0.72	0.73	0.73
	R_{LF}	45736	33353	34975

Table II: Response times (τ_{90}) in seconds for the sensor measured from the NO responses shown in Fig.7. The values represent the time required to achieve 90% of the steady state value after the gas composition is changed.

O_2 concentration, %	**t_{90}, seconds**		
	0 to 50 ppm*	**50 to 25 ppm***	**8 to 0 ppm***
2.0	5.5	3.0	2.6
7.0	5.4	1.0	6.3
10.5	4.1	3.2	3.7
18.9	4.7	2.5	5.8

*Change in NO concentration

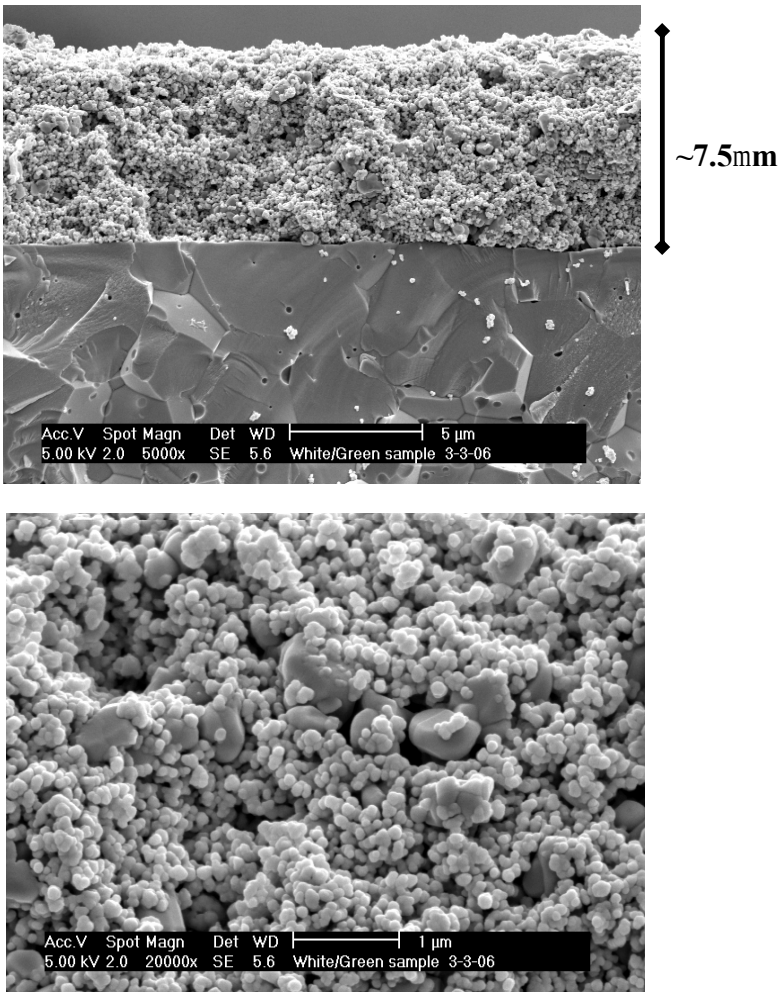

Fig. 1: SEM micrographs of a fracture surface from a YSZ/Cr_2O_3 composite electrode.

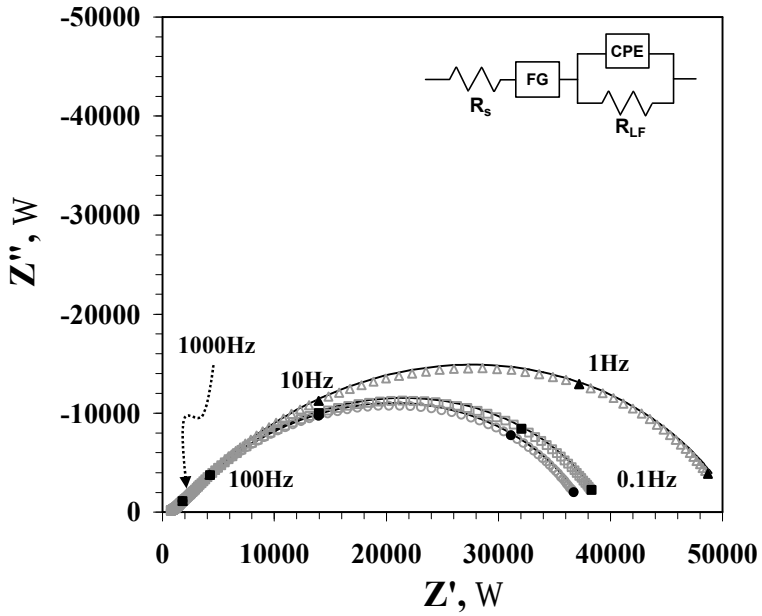

Fig. 2: Nyquist plot showing the impedance spectrum for the sensor at 600^{o}C in 10.5% O_2 (triangles), and in 10.5% O_2 mixed with 100 ppm NO (circles) and 100 ppm NO_2 (squares). Solid lines show the best fit for the equivalent circuit (inset)

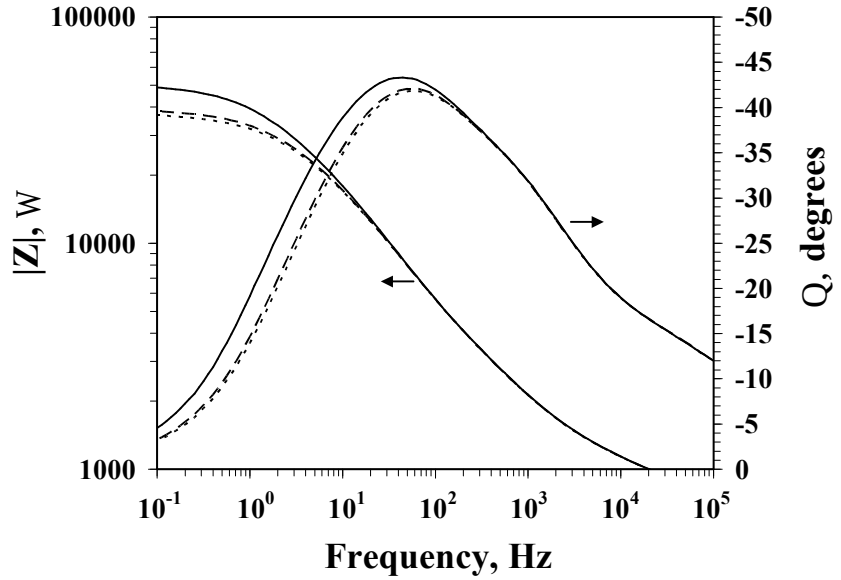

Fig. 3a: Bode plot of the impedance spectrum for the sensor at 600^{o}C in 10.5% O_2 (solid lines), and in 10.5% O_2 mixed with 100 ppm NO (dotted lines) and 100 ppm NO_2 (dashed lines).

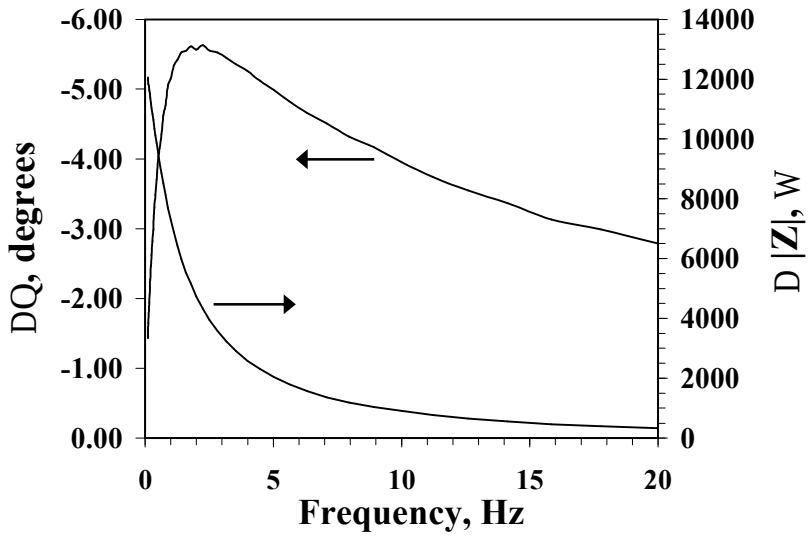

Fig. 3b: Difference between the Θ measured in 10.5% O_2, and in 10.5% O_2 mixed with 100 ppm NO, from Fig. 3a. Also shown, the difference between the |Z| measured in 10.5% O_2, and in 10.5% O_2 mixed with 100 ppm NO.

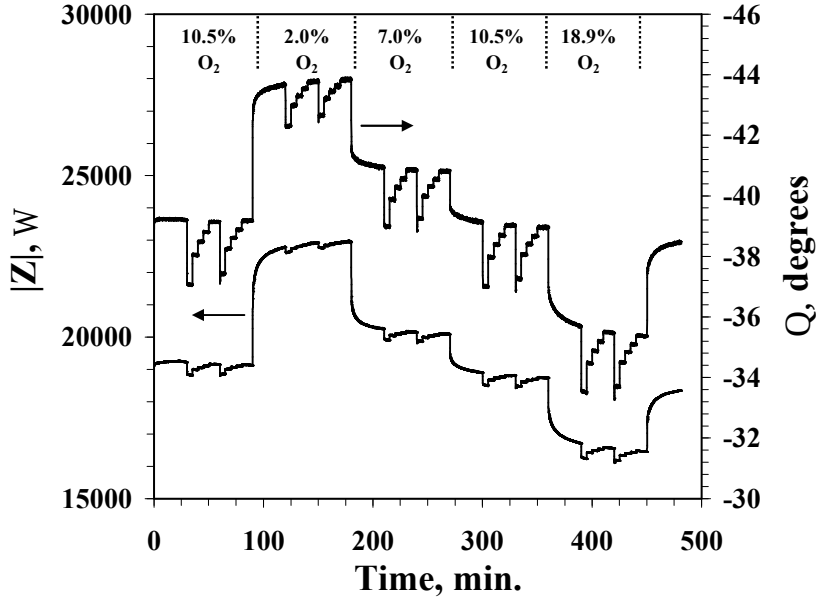

Fig. 4a: |Z| and Θ measured at 10 Hz and 600°C with an excitation voltage of 50 mV rms. The O_2 concentration varies from 2 -18.9%, and NO_x exposures of 50, 25, 15, and 8 ppm of NO (1^{st}) and NO_2 (2^{nd}) are performed at each concentration.

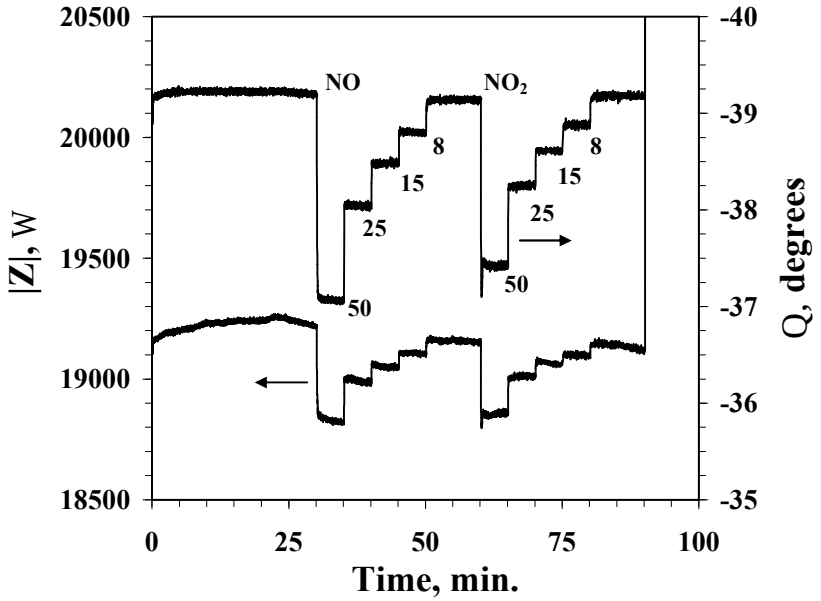

Fig. 4b: Expanded view of the 1st 100 minutes from Fig.3a. Shows |Z| and Θ measured at 10 Hz in 10.5% O_2. NO (1st) and NO_2 (2nd) concentrations are indicated in the Figure (50, 25, 15, and 8 ppm).

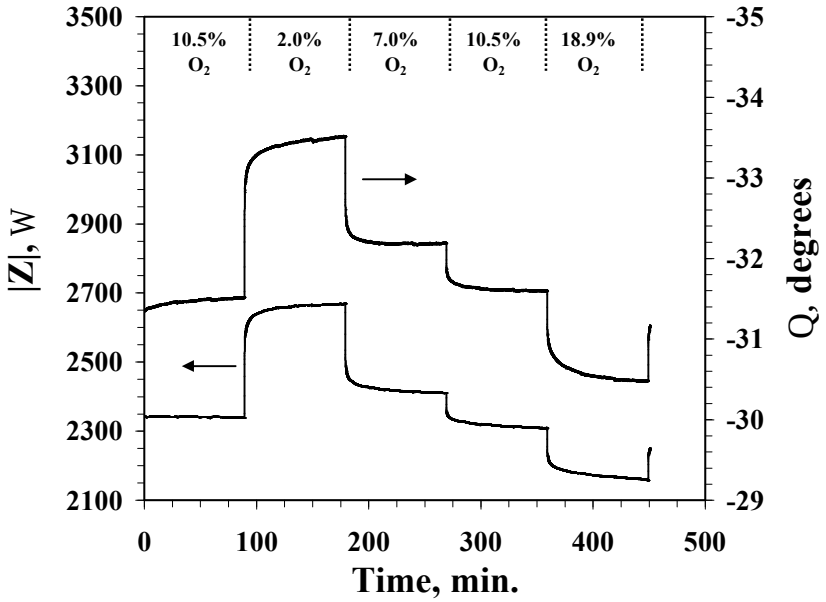

Fig. 5: |Z| and Θ measured at 1000 Hz and 600°C with an excitation voltage of 50 mV rms. The O_2 concentration varies from 2 -18.9%, and NO_x exposures of 50, 25, 15, and 8 ppm of NO (1^{st}) and NO_2 (2^{nd}) are performed at each concentration. The gas concentration profile (versus time) is exactly the same as in Fig. 4a.

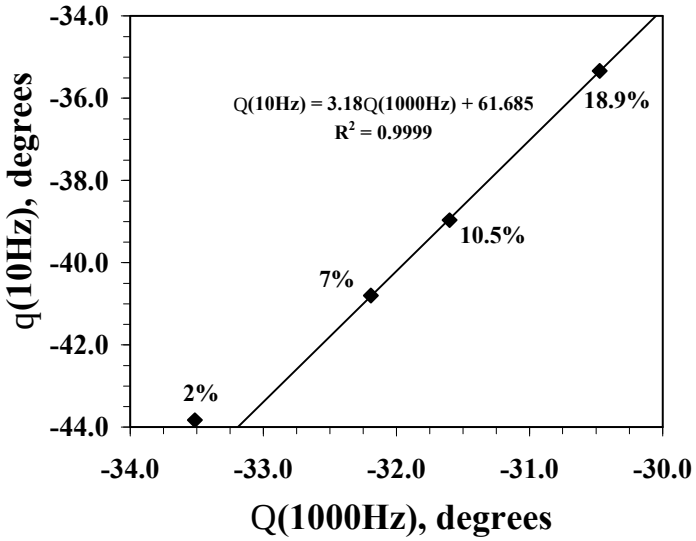

Fig. 6: Phase angle measured at 10 Hz, Θ(10 Hz), versus 1000 Hz, Θ(1000 Hz), for O_2 concentrations from 2 to 18.9%. The O_2 concentrations are indicated in the Figure. All measurements were made at 600^{o}C and 50 mV excitation voltage.

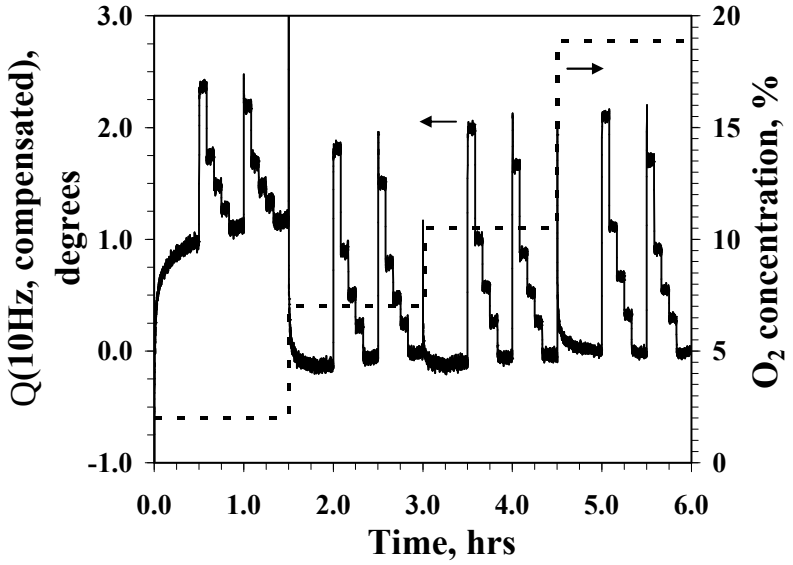

Fig. 7: Sensor response, Θ(10 Hz), from Fig. 4a compensated for the O_2 background using Θ(1000 Hz), versus from Fig. 5 and the linear correlation from Fig. 6.

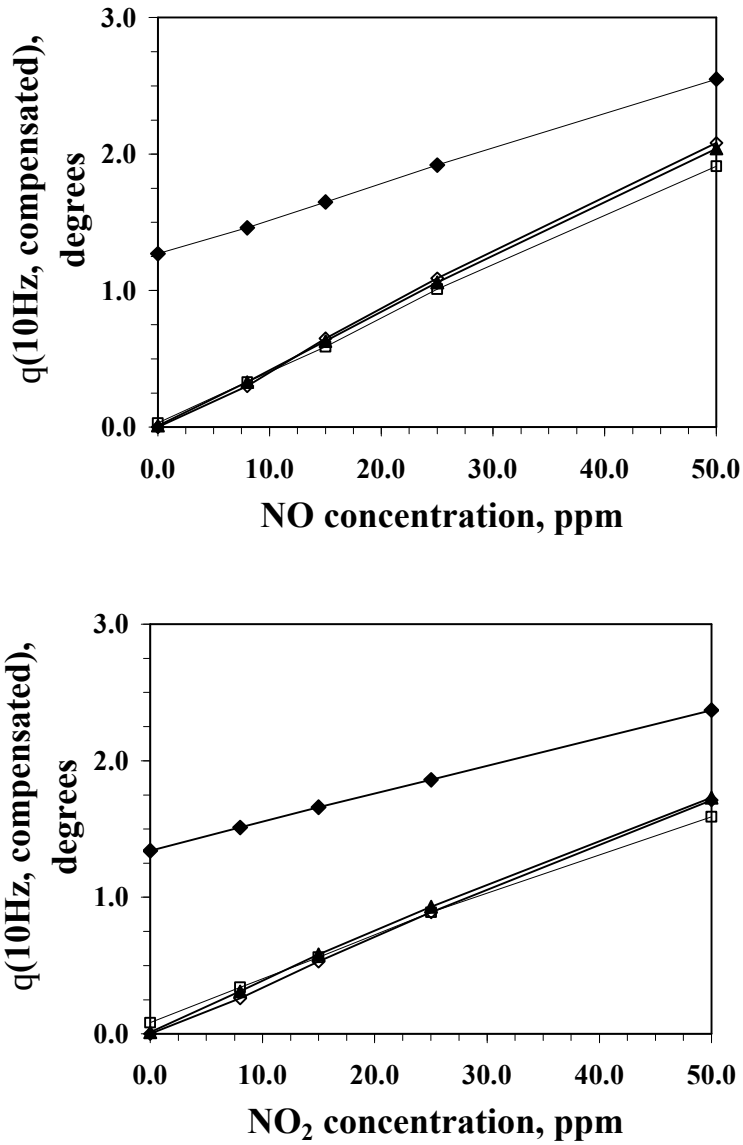

Fig. 8: Compensated sensor response from Fig. 7, Θ(10 Hz, compensated), compiled to illustrate (a) NO and (b) NO_2 response at O2 concentrations of 2% (filled diamonds), 7% (open squares), 10.5% (filled triangles), and 18.9% (open diamonds).

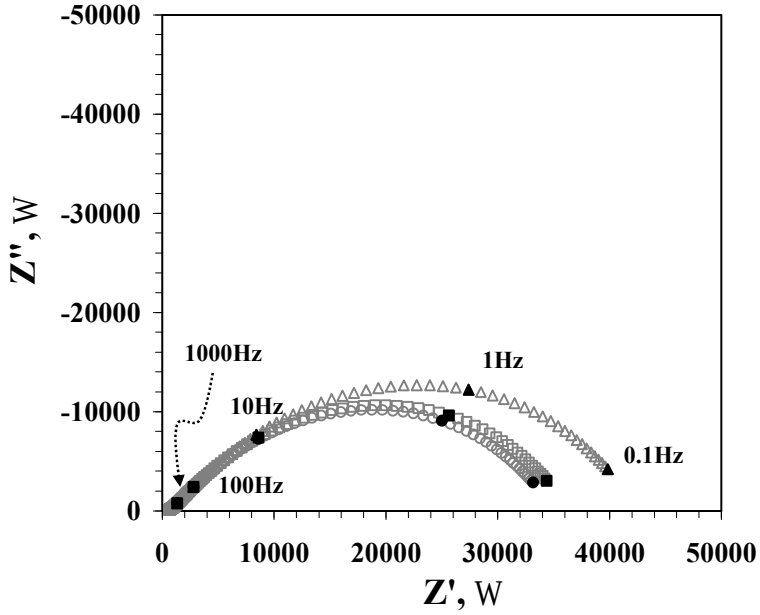

Fig. 9: Nyquist plot showing the impedance spectrum for the sensor at 600^{o}C in 10.5% O_2 (triangles), and in 10.5% O_2 mixed with 100 ppm NO (circles) and 100 ppm NO_2 (squares). The excitation voltage is 140 mV rms.

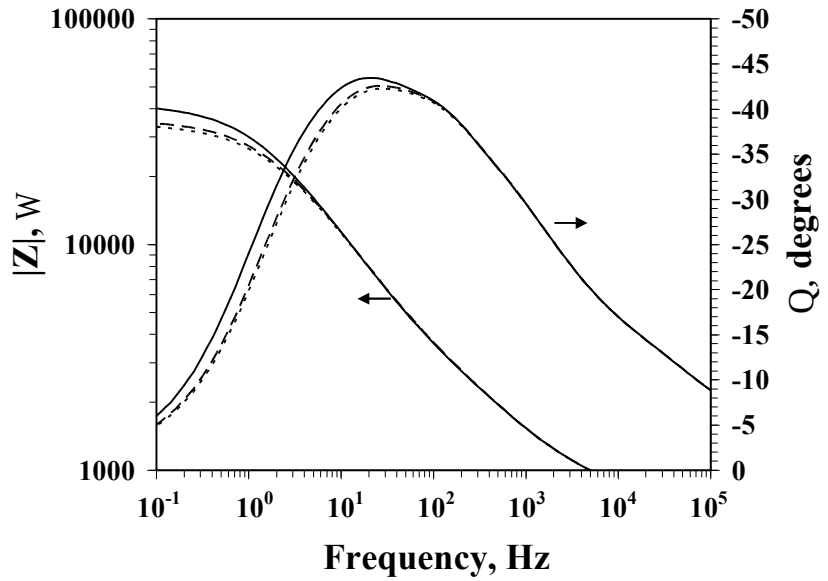

Fig. 10: Bode plot of the impedance spectrum for the sensor at 600°C in 10.5% O_2 (solid lines), and in 10.5% O_2 mixed with 100 ppm NO (dotted lines) and 100 ppm NO_2 (dashed lines). The excitation voltage is 140 mV rms.

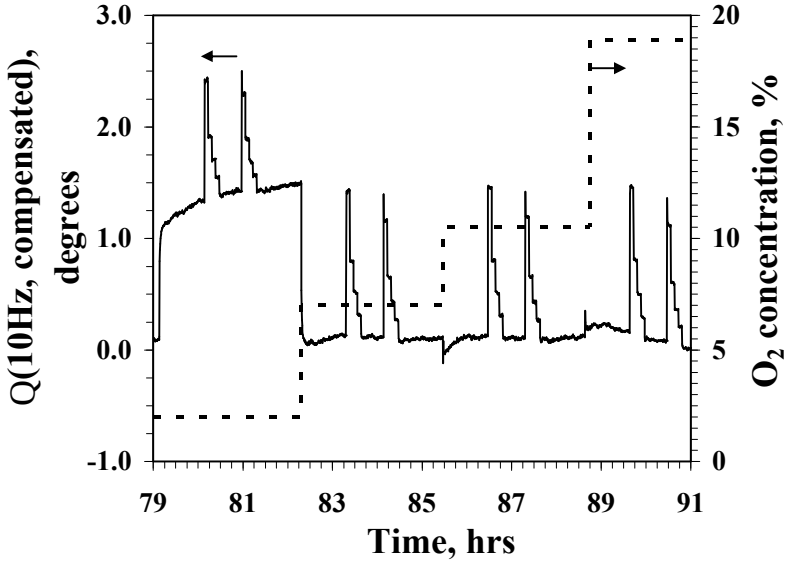

Fig. 11: Phase response at 10 Hz compensated for the O_2 background using Θ(1000 Hz) with an excitation voltage of 140 mV.

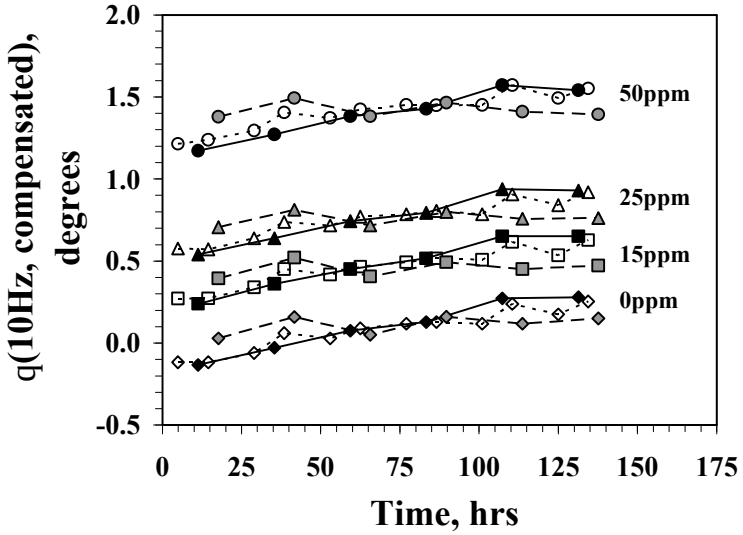

Fig. 12: O_2-compensated phase response during 140 hours of continuous operation with an excitation voltage of 140 mV. Response to 0, 15, 25, and 50 ppm NO (diamond, square, triangle, and circle, respectively) are shown for 7, 10.5 and 18.9% O_2 (filled, open, and grey symbols, respectively).